batteries

MDPI

Article

Multifunctional MXene–Fe_3O_4–Carbon Nanotube Composite Electrodes for High Active Mass Asymmetric Supercapacitors

Wenyu Liang [1], Rui Xu [1,*], Mohamed Nawwar [2] and Igor Zhitomirsky [3,*]

[1] School of Materials Science and Engineering, University of Science and Technology Beijing, Beijing 100083, China; liangw@ustb.edu.cn
[2] Technical Research Center (TRC), Cairo 12622, Egypt
[3] Department of Materials Science and Engineering, McMaster University, Hamilton, ON L8S 1L7, Canada
* Correspondence: ruixu@ustb.edu.cn (R.X.); zhitom@mcmaster.ca (I.Z.)

Abstract: $Ti_3C_2T_x$–Fe_3O_4–carbon nanotube composites were prepared for electrochemical energy storage in the negative electrodes of supercapacitors. The electrodes show a remarkably high areal capacitance of 6.59 F cm^{-2} in a neutral Na_2SO_4 electrolyte, which was obtained by the development of advanced nanofabrication strategies and due to the synergistic effect of the individual components. Enhanced capacitance was achieved using the in-situ synthesis method for the Fe_3O_4 nanoparticles. The superparamagnetic behavior of the Fe_3O_4 nanoparticles facilitated the fabrication of electrodes with a reduced binder content. Good mixing of the components was achieved using a celestine blue co-dispersant, which adsorbed on the inorganic components and carbon nanotubes and facilitated their co-dispersion and mixing. The capacitive behavior was optimized by the variation of the electrode composition and mass loading in a range of 30–45 mg cm^{-2}. An asymmetric device was proposed and fabricated, which contained a $Ti_3C_2T_x$–Fe_3O_4–carbon nanotube negative electrode and a polypyrrole–carbon nanotube positive electrode for operation in an Na_2SO_4 electrolyte. The asymmetric supercapacitor device demonstrated high areal capacitance and excellent power-density characteristics in an enlarged voltage window of 1.6 V. This investigation opens a new avenue for the synthesis and design of MXene-based asymmetric supercapacitors for future energy storage devices.

Keywords: MXene; iron oxide; superparamagnetism; polypyrrole; supercapacitor

check for updates

Citation: Liang, W.; Xu, R.; Nawwar, M.; Zhitomirsky, I. Multifunctional MXene–Fe_3O_4–Carbon Nanotube Composite Electrodes for High Active Mass Asymmetric Supercapacitors. *Batteries* **2023**, *9*, 327. https://doi.org/10.3390/batteries9060327

Academic Editor: Marco Giorgetti

Received: 7 April 2023
Revised: 6 June 2023
Accepted: 11 June 2023
Published: 16 June 2023

1. Introduction

Advanced energy storage technology is of significance today, due to the energy crises challenge worldwide [1–5]. MXenes have been extensively investigated as new energy storage materials [6–8] since their discovery in 2011 [9]. Due to their large surface area, good conductivity and rich surface chemistry, MXenes have demonstrated great potential for the development of high performance pseudocapacitors [10–13]. As the most widely studied material among the various types of MXenes, $Ti_3C_2T_x$ with the accordion-like particle shape contains alternation of Ti and C layers with a number of functional terminations, such as -O, -F and -OH [9].

Many efforts have been made to enhance the electrochemical performance of $Ti_3C_2T_x$ in composites with polymers [14–17], oxides [18–20], hydroxides [21,22] and carbon-based materials [23–25]. These studies showed that combining $Ti_3C_2T_x$ with other capacitive materials is a promising strategy for the development of advanced supercapacitor electrodes.

Fe-based materials, such as FeOOH, Fe_2O_3 and Fe_3O_4, exhibit high capacitance in a relatively large negative potential range [26–30]. Therefore, they have great potential to be considered as candidates for composites with MXene with enhanced electrochemical performance. Ma et al. [31] employed Fe_2O_3 nanoparticles intercalating flexible MXene hybrid paper and achieved an ultrahigh volumetric capacitance of 2607 F cm^{-3} as well as excellent cycling performance. In another research, a freestanding Ti_3C_2/FeOOH hybrid

film was designed in which amorphous FeOOH quantum dots acted as pillars to prevent restacking of MXene sheets [32]. A flexible electrode was fabricated by few-layered $Ti_3C_2T_x$ MXenes coupling with Fe_2O_3 nanorod arrays and grown on carbon cloth, which presented a remarkable areal capacitance of 725 mF cm^{-2} at a current density of 1 mA cm^{-2} [33]. It has been proven that MXene can provide iron oxides/hydroxides with efficient ion/electron transport pathways, so the electronic conductivity of the composites can be enhanced [34–36].

Although the tremendous efforts have been made to develop the advanced MXene electrodes with excellent electrochemical performance, very limited research paid attention to the significance of achieving high active mass loading (AML) of electrodes for supercapacitors [37–42]. For practical applications, the AML is required to be at least 10 to 20 mg cm^{-2} [43–45]. High AML is of great importance to reduce the relative mass of current collectors and other in-active components in the total mass of electrodes and devices. Designing of supercapacitors with high active mass loading will be beneficial to meet the demand of manufacturing. However, with increasing AML, the diffusion of electrolyte in the electrode and the conductivity will be drastically decreased. As the result, low capacitance and poor rate performance can be expected.

In this research, we fabricated MXene-Fe_3O_4-CNT anodes with high AML in the range of 30-45 mg cm^{-2}, optimized their composition and performance and application for the fabrication of asymmetric supercapacitor devices. Fe_3O_4 was selected because of its high theoretical capacitance(2299 F g^{-1}), earth abundance and low price [46]. Moreover, it exhibits advanced ferrimagnetic properties, which can be controlled by its particle size and synthetic strategy [47,48]. So Fe_3O_4 can impart magnetic properties to the composite materials. This offers benefits of reduced binder content in the composite electrodes and opens the gate for the fabrication of electrodes with advanced functionality. The successful synthesis of composite materials is based on the enhanced co-dispersion and improved mixing of different components, which can be attributed to the application of efficient dispersing agent celestine blue and advanced in-situ synthesis method. We analyzed the influence of electrode composition on electrochemical performance. The fabricated negative electrode showed high areal capacitance of 6.59 F cm^{-2} at a sweep rate of 2 mV s^{-1} at 40 mg cm^{-2} AML. Combining negative MXene-Fe_3O_4-carbon nanotube with positive polypyrrole (PPy)-MCNT electrode, we fabricated advanced asymmetric supercapacitor device working in enlarged voltage window of 1.6 V and showing high power-density characteristics.

2. Materials and Methods

2.1. Starting Materials

$FeCl_2 \cdot 4H_2O$, $FeCl_3 \cdot 6H_2O$, NH_4OH, celestine blue (CB), pyrrole (Py), pyrocatechol violet (PCV), ammonium persulfate (APS), sodium sulphate (Na_2SO_4) and poly (vinyl butyral-co-vinyl alcohol-co-vinyl acetate) (PVBAA, 65 kDa) were ordered from Millipore Sigma company. Multiwalled carbon nanotubes (MCNT, diameter = 13 nm, length = 1–2 µm) were purchased from Bayer Corporation. $Ti_3C_2T_x$ (BET surface area 5.03 m^2 g^{-1}) was supplied by Laizhou Kai Kai Ceramic Materials Co., Ltd., Weifang, China. Commercial Ni foam (surface area 2.01 m^2 g^{-1}, Vale) with 95% porosity was used as a current collector.

2.2. Synthesis of Composite Materials

In method 1, the synthesis procedure for Fe_3O_4 was similar to that described in a previous investigation [49]. Fe_3O_4 particles were precipitated from a solution containing Fe^{2+} and Fe^{3+} in a molar ratio of 1:2 at a temperature of 50 °C by adding 2 M NH_4OH for pH adjustment to pH = 9. After washing, vacuum filtration and drying in a furnace overnight at 60 °C, the powders were mixed with $Ti_3C_2T_x$ and MCNT in a mass ratio of 6:3:1 of $Ti_3C_2T_x$:Fe_3O_4:MCNT, and then dispersed in water using CB dispersant under probe sonication for 5 min.

Method 2 involved the in-situ synthesis of composites by the precipitation of Fe_3O_4 in the presence of co-dispersed $Ti_3C_2T_x$ and MCNT. The suspensions of $Ti_3C_2T_x$ and

MCNT were co-dispersed by CB under probe sonication, then combined with the solution containing Fe^{2+} and Fe^{3+} in a ratio of 1:2. The pH adjustment was achieved by injection of 2 M NH_4OH dropwise to 9, keeping the temperature at 50 °C. This was followed by washing, vacuum filtrating and drying processes; the powders were then ready for electrode preparation. The mass ratios between $Ti_3C_2T_x$, Fe_3O_4 and MCNT were 60:30:10, 55:30:15 and 55:25:20, and the obtained materials were named as $60Ti_3C_2T_x$–$30Fe_3O_4$–10MCNT, $55Ti_3C_2T_x$–$30Fe_3O_4$–15MCNT and $55Ti_3C_2T_x$–$25Fe_3O_4$–20MCNT, respectively.

The synthesis of polypyrrole(PPy)–MCNT composites followed a previous work [50]. In a typical procedure, 24 μL of pyrrole monomer was injected into the well-dispersed MCNT suspension for magnetic stirring for 5 h under 4 °C. The polymerization was achieved by addition of APS as the oxidant by a mass ratio APS:Py = 1:1. PCV was applied as a dopant for the polymerization of pyrrole and as a dispersant for MCNT, and the molar ratio was PCV:Py = 1:10. The precipitate was washed, vacuum filtrated and dried at room temperature.

2.3. Fabrication of Electrodes

The obtained materials were grinded into fine powders and used for preparation of slurries in ethanol containing 3% PVBAA binder, then impregnated into a commercial nickel foam current collector. The mass of active materials of electrodes was 30–45 mg cm^{-2}.

2.4. Characterization

The Quantum Design Magnetic Properties Measurement System was used to perform the magnetic measurements. The morphology study was performed by scanning electron spectroscopy (SEM) by JEOL JSM-7000F and transmission electron microscopy (TEM) by Talos 200X. EIS and CV were conducted by AMETEK 2273 potentiostat (Princeton). GCD was tested by Biologic AMP 300 potentiostat. For electrochemical testing, a 0.5 M Na_2SO_4 solution was applied as an electrolyte, and a Pt gauze and a saturated calomel electrode (SCE) were used as the counter and reference electrodes, respectively. For CV and GCD testing, the negative electrodes were tested in the potential range from −1.1 to −0.3 V. The potential range from −0.4 to +0.5 V was applied for positive electrode testing. The device was tested in a voltage window of 1.6 V. The mass- and areal-normalized capacitances (C_m and C_s, respectively) were calculated from the CV and GCD data according to the Equations (1)–(4):

$$\text{For CV,} \quad \text{Cm} = \frac{\int IdV}{2m\nu\Delta V} \tag{1}$$

$$\text{Cs} = \frac{\int IdV}{2A\nu\Delta V} \tag{2}$$

$$\text{For GCD,} \quad \text{Cm} = \frac{\int Idt}{m\Delta V} \tag{3}$$

$$\text{Cs} = \frac{\int Idt}{A\Delta V} \tag{4}$$

where I denotes current, V is potential, m is electrode active mass, ν stands for scan rate, A represents the area of electrode, ΔV is the potential range, and t is the discharge time.

EIS measurements of complex impedance Z* were performed at 5 mV AC signal and components of complex capacitance C* were obtained according to the Equations (5)–(8):

$$Z^* = Z' - iZ'' \tag{5}$$

$$C^* = C' - iC'' \tag{6}$$

$$C' = \frac{Z''}{\omega |Z|^2} \tag{7}$$

$$C' = \frac{Z'}{\omega |Z|^2} \tag{8}$$

where $\omega = 2\pi f$, f is frequency.

3. Results and Discussions

Fe_3O_4 is a ferrimagnetic material. Magnetic measurement of as-prepared Fe_3O_4 indicated its superparamagnetic behavior at room temperature (Figure 1). Such behaviour resulted from the use of small Fe_3O_4 particles. Magnetic particles facilitated the fabrication of the electrodes with reduced content of non-conductive binder. Moreover, magnetic particles added advanced functionality to the composite electrodes.

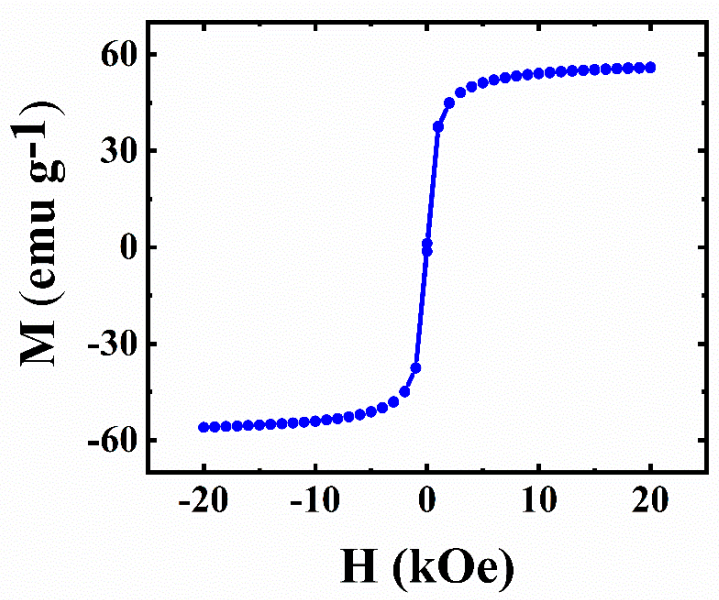

Figure 1. Magnetization (M) versus magnetic field (H) for Fe_3O_4.

The TEM images in Figure 2 show that the typical size of the as-synthesized Fe_3O_4 particles was about 10–15 nm, typically smaller than the superparamagnetic critical size of ~25 nm [47]. The small particle size explains the superparamagnetic behavior of Fe_3O_4. It is beneficial for particle dispersion and the fabrication of composites.

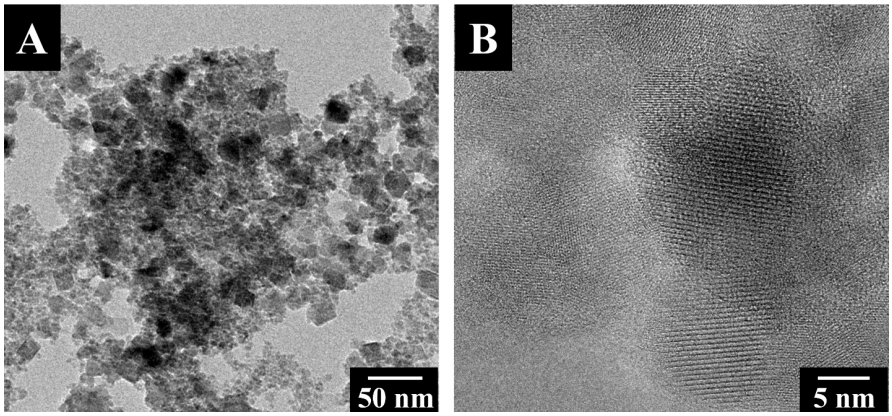

Figure 2. TEM images of Fe_3O_4 at (**A**) low and (**B**) high magnifications.

The electrode material prepared by method 1 was tested for its electrochemical performance in the potential range from −1.1 to −0.3 V. The testing results were plotted as shown in Figure 3. The CV graph in Figure 3A shows a nearly rectangular shape. The scan rate was increased from 2 to 100 mV s^{-1} and the capacitance was found to decrease (Figure 3B) from 2.42 to 0.55 F cm^{-2}. The capacitance retention at a high scan rate of 100 mV s^{-1} (R_{100}) was calculated to be 22.7%. The resistance of the electrode (Figure 3C), corresponding to the real part of Z*, was found to be 2.69 Ohms at a frequency of 10 mHz. The relatively low resistance achieved at 35 mg cm^{-2} mass loading indicated good conducting properties of the individual components. The C* dispersion of the relaxation type (Figure 3D) was observed and the relaxation frequency was 0.05 Hz, so a 20 s relaxation time constant could be calculated according to $\tau = 1/f$ from the C″ data. The charge and discharge curves were linear at 3–35 mA cm^{-2} current densities, showing good charge and discharge performance (Figure 3E). The capacitance was calculated as 2.42 F cm^{-2} at 3 mA cm^{-2} current density and decreased to 1.75 F cm^{-2} when the current density increased to 35 mA cm^{-2}, as shown in Figure 3F.

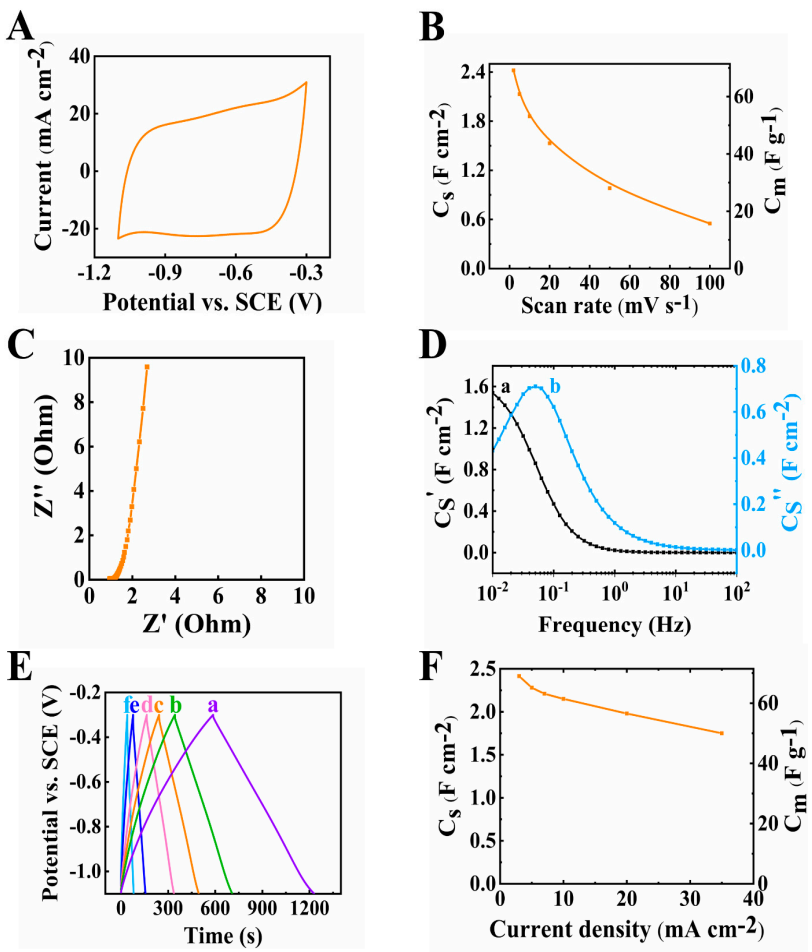

Figure 3. (**A**) Cyclic voltammetry data at 10 mV s^{-1} scan rate, (**B**) capacitance from CV data, (**C**) Nyquist plot of Z*, (**D**) complex capacitance from EIS data (a) Cs′ and (b) Cs″, (**E**) GCD plot at (a–f) 3, 5, 7, 10, 20 and 35 mA cm^{-2} and (**F**) capacitance from GCD data for $60Ti_3C_2T_x$-$30Fe_3O_4$-10MCNT electrode prepared by method 1 with mass of 35 mg cm^{-2}.

Method 2 offered the benefits of improved mixing of the components due to the in-situ synthesis of Fe_3O_4. It was demonstrated that the $60Ti_3C_2T_x$–$30Fe_3O_4$–10MCNT electrodes, prepared by method 2, showed notably higher specific capacitance, compared to the electrodes of the same composition, prepared by method 1. Moreover, the $55Ti_3C_2T_x$–$30Fe_3O_4$–15MCNT and $55Ti_3C_2T_x$–$25Fe_3O_4$–20MCNT electrodes, were prepared by method

2 and tested for comparison. CB was applied as a co-dispersant for $Ti_3C_2T_x$ and MCNT. The adsorption of the CB molecules on MCNT can be promoted by the polyaromatic structure of CB [51]. Moreover, the catechol group of CB facilitated its adsorption on $Ti_3C_2T_x$ and Fe_3O_4 by creating bidentate chelating or bridging bonds with the Ti and Fe atoms on the material surfaces. The morphologies of the materials prepared by method 2 were studied by SEM and presented in Figure 4. It can be seen that MCNT and Fe_3O_4 were formed between the open layers of $Ti_3C_2T_x$ and on the $Ti_3C_2T_x$ surface. This resulted in improved mixing of the electrode components.

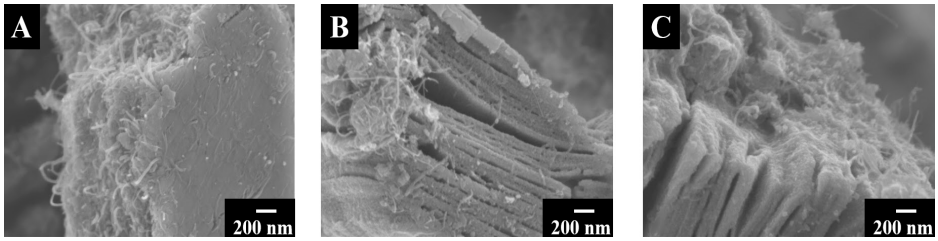

Figure 4. SEM images of (**A**) $60Ti_3C_2T_x$–$30Fe_3O_4$–10MCNT, (**B**) $55Ti_3C_2T_x$–$30Fe_3O_4$–15MCNT and (**C**) $55Ti_3C_2T_x$–$25Fe_3O_4$–20MCNT powders prepared by method 2.

The $60Ti_3C_2T_x$–$30Fe_3O_4$–10MCNT, $55Ti_3C_2T_x$–$30Fe_3O_4$–15MCNT and $55Ti_3C_2T_x$–$25Fe_3O_4$–20MCNT, electrodes with an AML of 35 mg cm^{-2} fabricated by method 2 were studied for their electrochemical performance. Figure 5 shows the CV and EIS results. The largest CV area was acquired for the $60Ti_3C_2T_x$–$30Fe_3O_4$–10MCNT electrode, indicating the highest capacitance. The capacitances at 2 mV s^{-1} scan rate were calculated to be 5.44, 4.92 and 4.62 F cm^{-2} for the $60Ti_3C_2T_x$–$30Fe_3O_4$–10MCNT, $55Ti_3C_2T_x$–$30Fe_3O_4$–15MCNT and $55Ti_3C_2T_x$–$25Fe_3O_4$–20MCNT electrodes, respectively. The equivalent circuit (Figure S1) developed for the high AML electrodes was used for the impedance spectroscopy [52]. The R_t values were calculated to be 0.65, 0.62 and 0.93 for the $60Ti_3C_2T_x$–$30Fe_3O_4$–10MCNT, $55Ti_3C_2T_x$–$30Fe_3O_4$–15MCNT and $55Ti_3C_2T_x$–$25Fe_3O_4$–20MCNT electrodes, respectively. The relatively low impedance was achieved at high AML of 35 mg cm^{-2}, which indicated low resistance and high capacitance. The Bode modulus are provided in Figure S2. In Figure 5D,E, the relaxation type dispersion was observed for these electrodes.

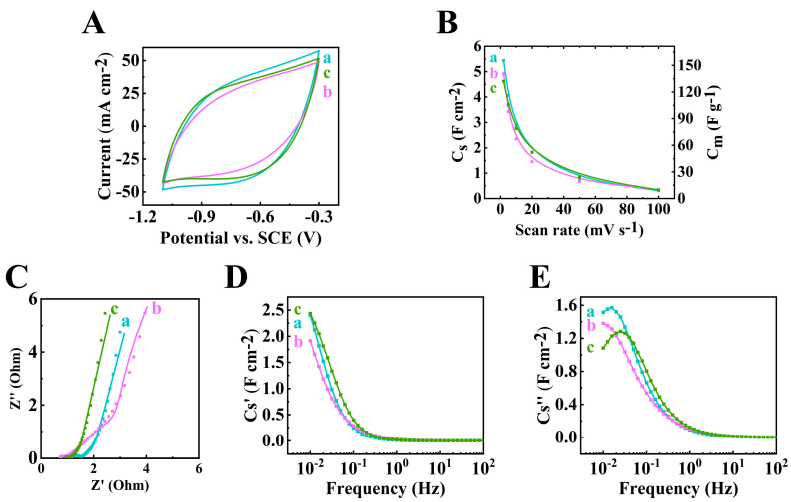

Figure 5. (**A**) Cyclic voltammetry at 10 mV s^{-1}, (**B**) capacitance acquired from CV measurement, (**C**) Nyquist plot of Z* ((•) experimental data and (–) simulation data), (**D**,**E**) components of complex capacitance: (**D**) Cs′ and (**E**) Cs″ for (a) $60Ti_3C_2T_x$–$30Fe_3O_4$–10MCNT, (b) $55Ti_3C_2T_x$–$30Fe_3O_4$–15MCNT and (c) $55Ti_3C_2T_x$–$25Fe_3O_4$–20MCNT electrodes prepared by method 2 with AML of 35 mg cm^{-2}.

The pseudocapacitive behaviour of $Ti_3C_2T_x$ is related to the oxidation state change between Ti^{4+}/Ti^{3+}, following the bonding and de-bonding of the oxygen group [53], as described by Equation (9). The electrochemical reaction of Fe_3O_4 can be attributed to the redox reaction between Fe^{3+}/Fe^{2+}, accompanying with the intercalation of Na^+ ions [54], as shown in Equation (10).

$$Ti_3C_2O_X(OH)_yF_z + \delta Na^+ + \delta e^- \leftrightarrow Na_\delta Ti_3C_2O_X(OH)_yF_z \quad (9)$$

$$Fe_3O_4 + \delta Na^+ + \delta e^- \leftrightarrow Na_\delta Fe_3O_4 \quad (10)$$

The contribution of surface and intercalation capacitances to the total energy storage by the composite electrodes was analyzed using the Dunn's method [55–57]. A critical parameter b was applied to indicate the energy storage mechanism: for battery-type materials with diffusion-controlled capacitance, b = 0.5, and for purely double-layer capacitors with surface-controlled behaviour, b = 1 [58]. For materials with 0.5 < b < 0.8, the battery-type energy storage was dominant [59]. The b-value of as-prepared composites were determined to be 0.60, 0.56 and 0.62 for the $60Ti_3C_2T_x$–$30Fe_3O_4$–10MCNT, $55Ti_3C_2T_x$–$30Fe_3O_4$–15MCNT and $55Ti_3C_2T_x$–$25Fe_3O_4$–20MCNT electrodes, respectively (Figure S3). Therefore, the composite electrodes showed a mixed energy storage mechanism with a dominant battery-type behaviour.

Figure 6 demonstrates the GCD results of the composite electrodes. The linear shapes of all the curves at different current densities indicated good pseudocapacitive performance. The longest charge–discharge time was obtained for the $60Ti_3C_2T_x$–$30Fe_3O_4$–10MCNT sample, due to its highest capacitance. The decrease of capacitance was observed for all the electrodes when current was increased, as shown in Figure 6D. Based on the testing results above, the electrode of $60Ti_3C_2T_x$–$30Fe_3O_4$–10MCNT showed the best performance with the highest capacitance and relatively low impedance at a high mass loading.

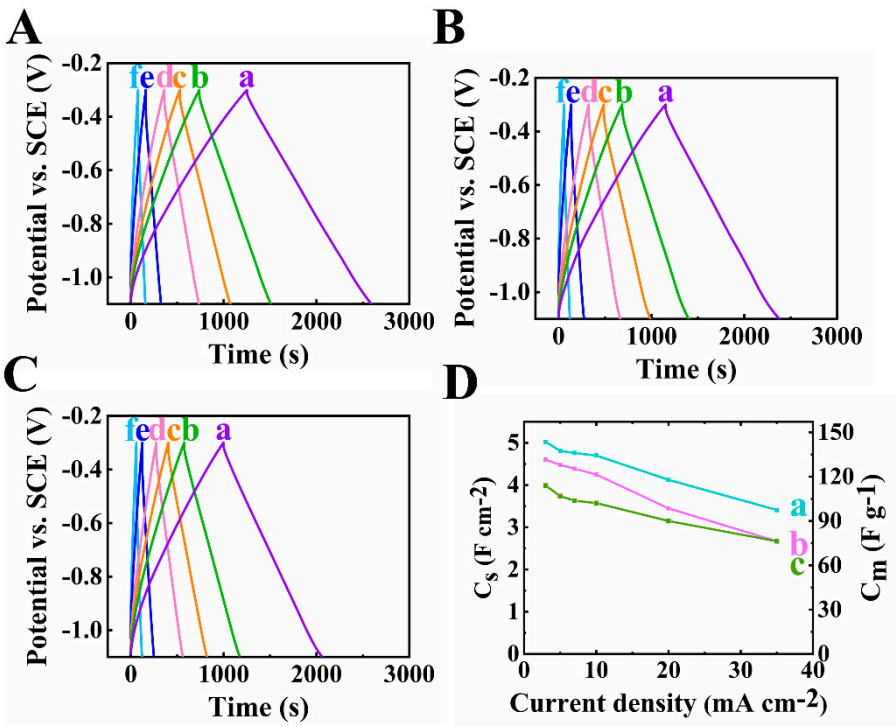

Figure 6. (**A**–**C**) Galvanostatic charge discharge plots at scan rates of (a-f)3,5,7,10,20 and 35 mA cm^{-2} of (**A**) $60Ti_3C_2T_x$–$30Fe_3O_4$–10MCNT, (**B**) $55Ti_3C_2T_x$–$30Fe_3O_4$–15MCNT and (**C**) $55Ti_3C_2T_x$–$25Fe_3O_4$–20MCNT, (**D**) capacitance calculated from GCD data of (a) $60Ti_3C_2T_x$–$30Fe_3O_4$–10MCNT, (b) $55Ti_3C_2T_x$–$30Fe_3O_4$–15MCNT and (c) $55Ti_3C_2T_x$–$25Fe_3O_4$–20MCNT electrodes prepared by method 2 with AML of 35 mg cm^{-2}.

The active mass is another important factor of supercapacitor electrodes. Recent research emphasized the significance of high active mass loading of electrodes for practical applications [51]. With the increasing AML of an electrode, the performance can be drastically hindered due to the inefficient diffusion of electrolyte ions. To optimize the pseudocapacitive performance, electrodes with different AML from 30 to 45 mg cm^{-2} of 60$Ti_3C_2T_x$–30Fe_3O_4–10MCNT were fabricated and tested. The testing results were compared, as shown in Figure 5 (a) and Figure 7. As shown in Figure 7A, the largest CV area was found for the electrode at 40 mg cm^{-2} mass loading, indicating its highest capacitance. The areal capacitances calculated from the CV data were found to be 4.18 F cm^{-2}, 5.44 F cm^{-2}, 6.59 F cm^{-2} and 5.89 F cm^{-2}, for mass loadings at 30, 35, 40 and 45 mg cm^{-2}, respectively at scan rate of 2 mV s^{-1}. From the EIS results shown in Figure 5C–E (a) and Figure 7C–E, the lowest resistance related to Z′ and the highest real capacitance C′ were achieved for the 40 mg cm^{-2} electrode.

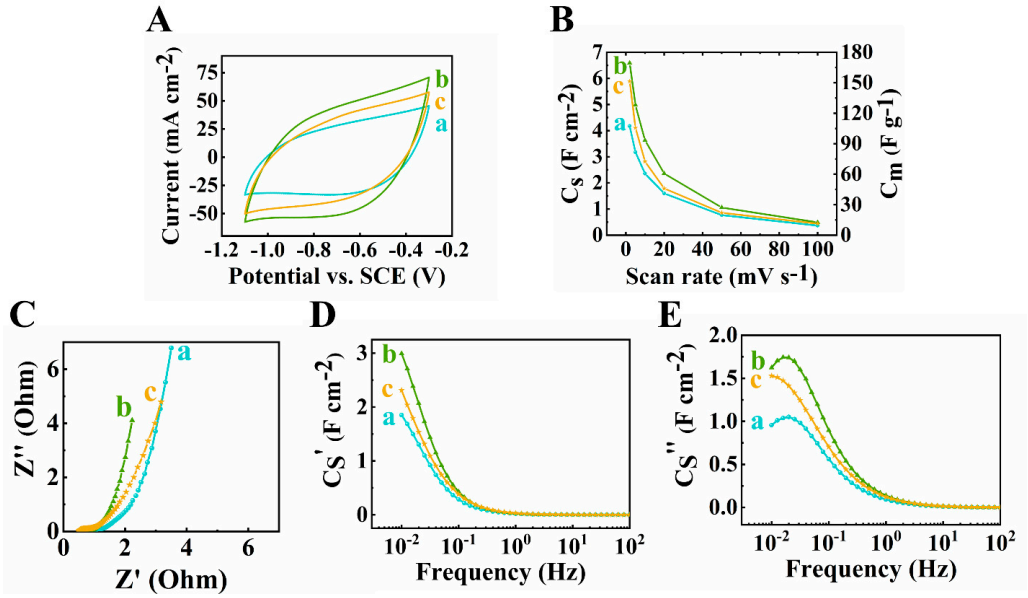

Figure 7. (**A**) Cyclic voltammetry at 10 mV s^{-1} scan rate, (**B**) capacitance from CV data, (**C**) Nyquist plot, (**D**,**E**) complex capacitance components (**D**) Cs′ and (**E**) Cs″ of 60$Ti_3C_2T_x$–30Fe_3O_4–10MCNT electrodes at (a) 30, (b) 40 and (c) 45 mg cm^{-2} active mass loading electrodes prepared by method 2.

The GCD results shown in Figures 6A and 8 are consistent with the CV and EIS data. Good pseudocapacitive performance was proven by the triangular-shaped curves. The longest discharge time was obtained for the electrode at 40 mg cm^{-2} mass loading, which is the result of its highest capacitance.

Fabrication of an advanced asymmetric supercapacitor requires a high-performance positive electrode exhibiting comparable capacitance in an overlapping voltage window with the negative electrode. The PPy–MCNT electrode was tested in a −0.4–+0.5 V potential range and showed a capacitance of 4.65 F cm^{-2} at scan rate of 2 mV s^{-1}. The rectangular-shaped CV curves, low impedance achieved at high mass loading and nearly linear GCD curves showed in Figure 9 confirmed the good capacitive properties of the PPy–MCNT positive electrode and as a result allowed the design of an asymmetric device.

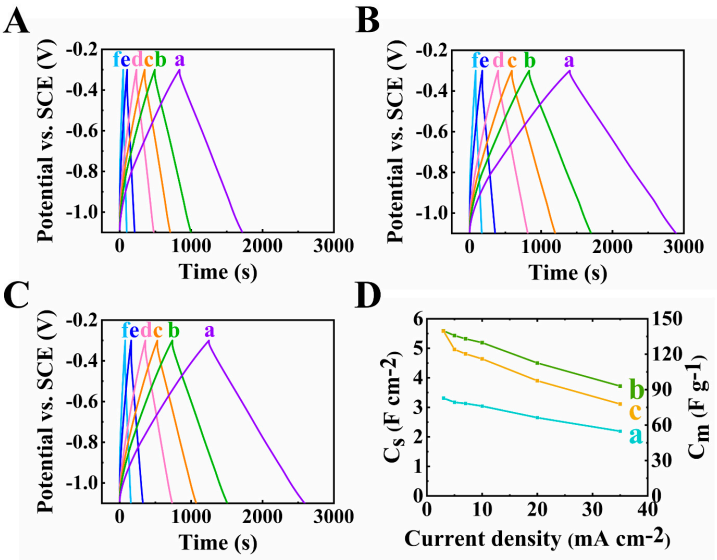

Figure 8. (**A**–**D**) GCD plots at scan rates of (a–f)3,5,7,10,20 and 35 mA cm^{-2} of $60Ti_3C_2T_x$–$30Fe_3O_4$–10MCNT electrodes at (**A**) 30, (**B**) 40 and (**C**) 45 mg cm^{-2} active mass loading and (**D**) capacitance from GCD data of $60Ti_3C_2T_x$–$30Fe_3O_4$–10MCNT electrodes at (a) 30, (b) 40 and (c) 45 mg cm^{-2} active mass loading electrodes prepared by method 2.

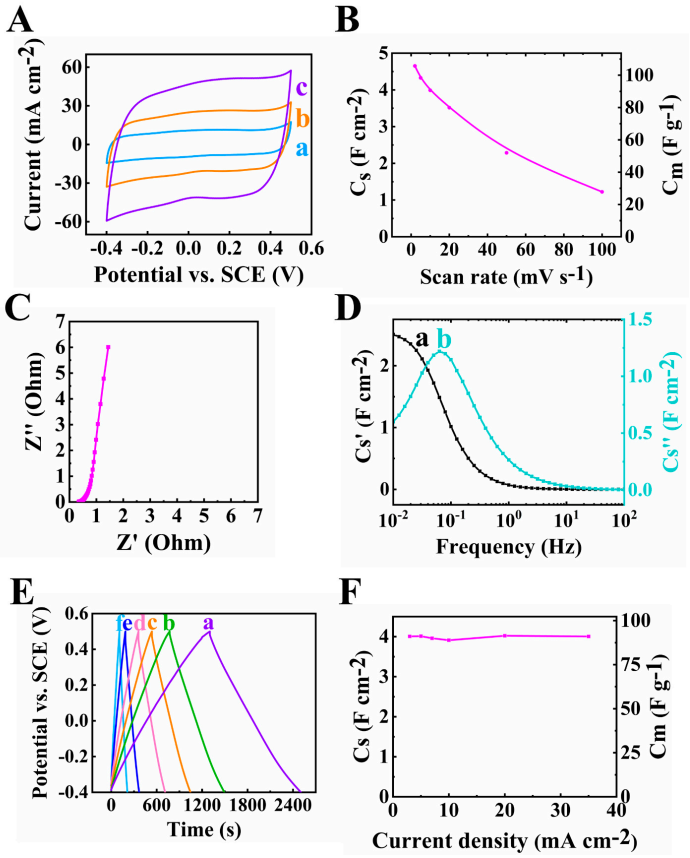

Figure 9. (**A**) Cyclic voltammetry data at (a) 5, (b) 10 and (c) 20 mV s^{-1} scan rate, (**B**) capacitance from CV data, (**C**) Nyquist plot of Z*, (**D**) complex capacitance from EIS data (a) Cs′ and (b) Cs″, (**E**) GCD plot at (a) 3,(b) 5, (c) 7, (d) 10, (e) 20 and (f) 35 mA cm^{-2} and (**F**) capacitance from GCD data for PPy–MCNT positive electrode.

The as-assembled asymmetric supercapacitor device contained $60Ti_3C_2T_x$–$30Fe_3O_4$–10MC-NT-40 mg as a negative electrode and PPy–MCNT as a positive electrode. The charge and mass balances were achieved as described in reference [51]. Briefly, the mass of the cathode and anode should follow the charge conservation principle:

$$Q = m + C + V + = m - C - V- \quad (11)$$

where $m+$ and $m-$ are the active mass of the cathode and anode, $C+$ and $C-$ represent the capacitance of the cathode and anode, and $V+$ and $V-$ are the potential range of the cathode and anode, respectively.

As shown in Figure 10, both the positive and negative electrodes showed good capacitive behavior in the overlapping potential windows, which is of significant importance for the successful development of an asymmetric device.

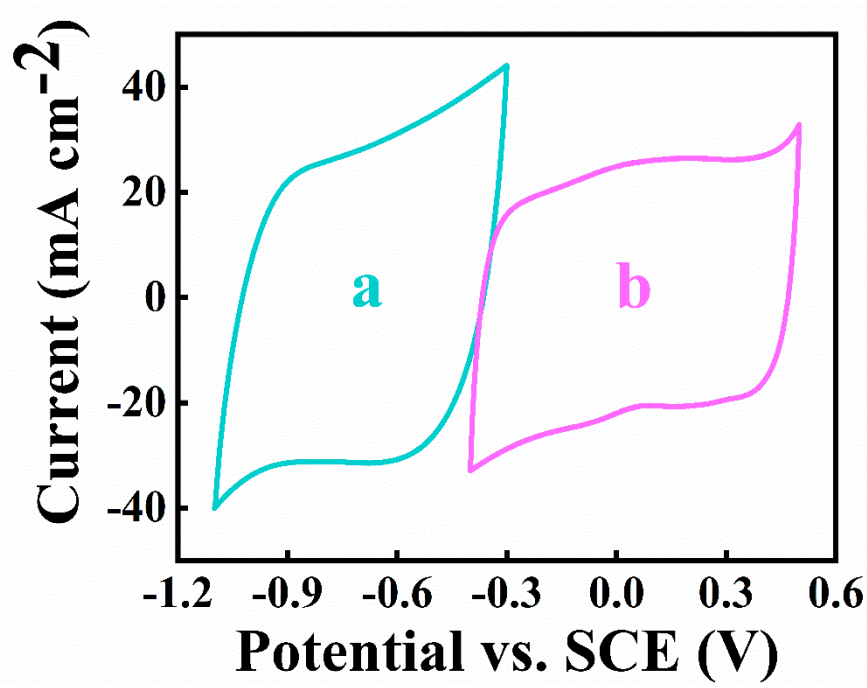

Figure 10. CVs at 5 mV s^{-1} scan rate for (a)negative and (b)positive electrodes.

The as-fabricated asymmetric supercapacitor was tested in an enlarged voltage window of 1.6 V. An areal capacitance as high as 1.96 F cm^{-2} was obtained at a 2 mV s^{-1} scan rate from the CV (Figure 11A,B) and 1.49 F cm^{-2} was obtained at 10 mA cm^{-2} current density from the GCD (Figure 12A,B). The total resistance for the device at high active mass loading (Figure 11C) depended on the resistances, related to the ion diffusion in the pores of both the electrodes and a membrane. The Cs′ value was obtained as 0.77 F cm^{-2} at the frequency of 0.01 Hz (Figure 11D).

The Ragone plot in Figure 12C showed that good power-energy characteristics were achieved in this investigation. The highest power density obtained from the device was 223.17 W m^{-2} (305.53 W kg^{-1}) and the highest energy density was determined as 4.34 Wh m^{-2} (5.94 Wh kg^{-1}). Cycling behaviour studies showed that the cell maintained 80% capacitance after 1000 CV cycles at scan rate of 50 mV s^{-1} (Figure 12D). It is suggested that the reduction of capacitance during cycling was not related to reduction of capacitance of the negative electrode. The investigation of cycling behavior of the negative electrode (Supplementary information, Figure S4) showed that the capacitance increased during 1000 cycles with a capacitance retention of 112%. The suggested mechanism of the capacitance increase was ascribed to microstructure changes of the electrode during cycling, as was observed in other investigations [60]. Therefore, the cycling performance of the device could be enhanced by the improvement of cycling stability of PPy–MCNT electrode.

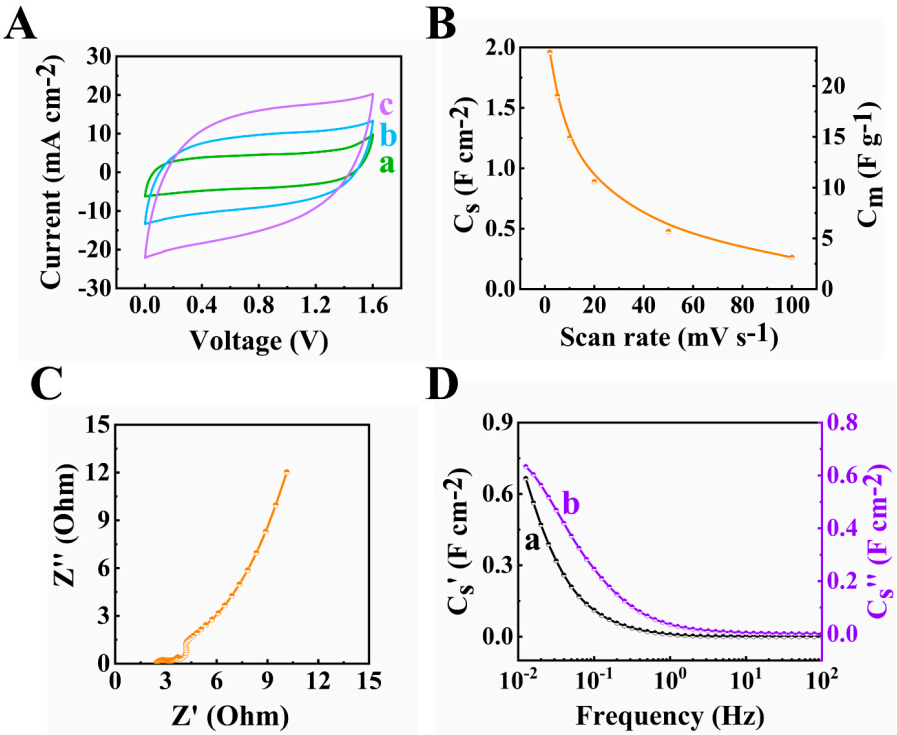

Figure 11. (**A**) CVs at (a–c) 2, 5 and 10 mV s^{-1} scan rates, (**B**) capacitance acquired from CV data, (**C**) Nyquist plot of Z* and (**D**) components of complex capacitance calculated from EIS data for the asymmetric device.

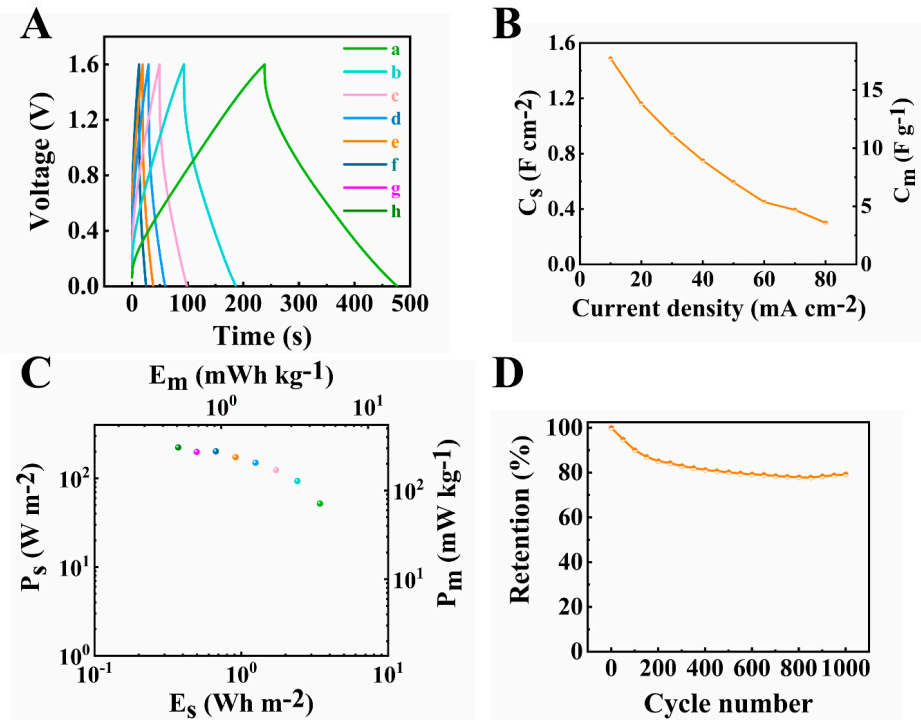

Figure 12. (**A**) Galvanostatic charge–discharge results at (a–h) 10, 20, 30, 40, 50, 60, 70 and 80 mA cm^{-2} current densities, (**B**) capacitance calculated from GCD data, (**C**) Ragone plot derived from GCD data(corresponding to curve h-a in Figure 12A from left to right dots) and (**D**) capacitance retention of the asymmetric device.

4. Conclusions

$Ti_3C_2T_x$–Fe_3O_4–MCNT electrodes were prepared for applications in the anodes of asymmetric supercapacitors with high capacitance and high loading. As-prepared Fe_3O_4 in the $Ti_3C_2T_x$–Fe_3O_4–MCNT composite material showed superparamagnetic properties due to the small particle size. The use of Fe_3O_4 imparted magnetic properties to the composite and allowed for the fabrication of an anode with low binder content, which was the key to achieving the high loading feature. The in-situ synthesis method allowed for significant improvement in the capacitance. The capacitive behavior of the electrodes prepared by the in-situ synthesis was optimized by variation of the composition and AML. The catecholate type co-dispersant with polyaromatic structure is beneficial for adsorption on MCNT, at the same time it can form bidentate chelating or bridging bonding on the $Ti_3C_2T_x$ and Fe_3O_4 surface. The strong adsorption and efficient co-dispersion facilitated the in-situ synthesis approach. The composite material containing 60% $Ti_3C_2T_x$, 30% Fe_3O_4 and 10% MCNT showed a remarkably high capacitance of 6.59 F cm^{-2} at a scan rate of 2 mV s^{-1} and low impedance at a high mass loading of 40 mg cm^{-2}. The key factors for achieving such high capacitance were the use of the in-situ synthesis method and celestine blue as a co-dispersant, reduced binder content and optimization of the composition and mass loading. The outstanding capacitive properties of composites render them a potential candidate for negative electrodes for asymmetric supercapacitors. The advanced asymmetric supercapacitor with a negative electrode of $60Ti_3C_2T_x$–$30Fe_3O_4$–10MCNT and a positive electrode of PPy–MCNT was fabricated, which exhibited superior electrochemical performance in an enlarged voltage window of 1.6 V. The optimal MXene-based electrode and advanced asymmetric supercapacitor showed great potential for future applications of commercial energy storage devices.

Supplementary Materials: The following supporting information can be downloaded at: https://www.mdpi.com/article/10.3390/batteries9060327/s1. Figure S1. Equivalent circuit developed from high active mass loading electrodes. R-C(Q) transmission line was combined in series with solution resistance R_s. R_n elements represented electrolyte resistance. Q was related to the constant phase elements and W stood for Warburg impedance. Double layer capacitance C_{dl} was in parallel with the charge transfer resistance R_t. Figure S2. Bold modulus of (A) impedance and (B) phase angle plot for (a) $60Ti_3C_2T_x$-$30Fe_3O_4$-10MCNT, (b) $55Ti_3C_2T_x$-$30Fe_3O_4$-15MCNT and (c) $55Ti_3C_2T_x$-$25Fe_3O_4$-20MCNT electrodes prepared by method 2 with AML of 35 mg cm^{-2}. Figure S3. Current (i) versus scan rate (ν) dependence in a logarithmic scale used for the calculation of b value by equation $i=av^b$ for (a) $60Ti_3C_2T_x$-$30Fe_3O_4$-10MCNT, (b) $55Ti_3C_2T_x$-$30Fe_3O_4$-15MCNT and (c) $55Ti_3C_2T_x$-$25Fe_3O_4$-20MCNT electrodes prepared by method 2 with AML of 35 mg cm^{-2}. Figure S4. Cycling stability of $60Ti_3C_2T_x$-$30Fe_3O_4$-10MCNT electrode at 40 mg cm^{-2} from CV at scan rate of 50 mV s^{-1}. Table S1. Capacitance (F cm^{-2}) and capacity (mAh g^{-1}) for as-prepared electrodes, calculated from CV data at 2 mV s^{-1} scan rate. Table S2. Summary of electrochemical performance of $Ti_3C_2T_x/Fe_3O_4$-based composite anode for supercapacitors. References [49,61,62] are cited in Supplementary Materials.

Author Contributions: Conceptualization, W.L. and I.Z.; methodology, W.L. and I.Z.; formal analysis, W.L. and M.N.; investigation, W.L.; writing—original draft preparation, W.L. and I.Z.; writing—review and editing, W.L., R.X. and I.Z.; supervision, I.Z.; project administration, I.Z.; funding acquisition, I.Z. All authors have read and agreed to the published version of the manuscript.

Funding: This research was funded by NSERC Canada.

Data Availability Statement: All data are available through the manuscript.

Acknowledgments: We acknowledge Canadian Centre for Electron Microscopy.

Conflicts of Interest: The authors declare no conflict of interest.

References

1. Mariappan, V.K.; Krishnamoorthy, K.; Manoharan, S.; Pazhamalai, P.; Kim, S.J. Electrospun Polymer-Derived Carbyne Supercapacitor for Alternating Current Line Filtering. *Small* **2021**, *17*, 2102971. [CrossRef]
2. Tian, J.; Cui, N.; Chen, P.; Guo, K.; Chen, X. High-Performance Wearable Supercapacitors Based on PANI/N-CNT@CNT Fiber with a Designed Hierarchical Core-Sheath Structure. *J. Mater. Chem. A Mater.* **2021**, *9*, 20635–20644. [CrossRef]
3. Gonçalves, J.M.; da Silva, M.I.; Toma, H.E.; Angnes, L.; Martins, P.R.; Araki, K. Trimetallic Oxides/Hydroxides as Hybrid Supercapacitor Electrode Materials: A Review. *J. Mater. Chem. A Mater.* **2020**, *8*, 10534–10570. [CrossRef]
4. Yewale, M.A.; Jadhvar, A.A.; Kharade, R.B.; Kadam, R.A.; Kumar, V.; Nakate, U.T.; Shelke, P.B.; Bobade, D.H.; Teli, A.M.; Dhas, S.D.; et al. Hydrothermally Synthesized Ni3V2O8 Nanoparticles with Horny Surfaces for HER and Supercapacitor Application. *Mater. Lett.* **2023**, *338*, 134033. [CrossRef]
5. Yewale, M.A.; Jadhavar, A.A.; Kadam, R.A.; Velhal, N.B.; Nakate, U.T.; Teli, A.M.; Shin, J.C.; Nguyen, L.N.; Shin, D.K.; Kaushik, N.K. Hydrothermal Synthesis of Manganese Oxide (Mn_3O_4) with Granule-like Morphology for Supercapacitor Application. *Ceram. Int.* **2022**, *48*, 29429–29437. [CrossRef]
6. Zhang, X.; Zhang, Z.; Zhou, Z. MXene-Based Materials for Electrochemical Energy Storage. *J. Energy Chem.* **2018**, *27*, 73–85. [CrossRef]
7. Nan, J.; Guo, X.; Xiao, J.; Li, X.; Chen, W.; Wu, W.; Liu, H.; Wang, Y.; Wu, M.; Wang, G. Nanoengineering of 2D MXene-Based Materials for Energy Storage Applications. *Small* **2021**, *17*, 1902085. [CrossRef] [PubMed]
8. Li, K.; Liang, M.; Wang, H.; Wang, X.; Huang, Y.; Coelho, J.; Pinilla, S.; Zhang, Y.; Qi, F.; Nicolosi, V.; et al. 3D MXene Architectures for Efficient Energy Storage and Conversion. *Adv. Funct. Mater.* **2020**, *30*, 2000842. [CrossRef]
9. Naguib, M.; Kurtoglu, M.; Presser, V.; Lu, J.; Niu, J.; Heon, M.; Hultman, L.; Gogotsi, Y.; Barsoum, M.W. Two-Dimensional Nanocrystals Produced by Exfoliation of Ti_3AlC_2. *Adv. Mater.* **2011**, *23*, 4248–4253. [CrossRef]
10. Boota, M.; Anasori, B.; Voigt, C.; Zhao, M.Q.; Barsoum, M.W.; Gogotsi, Y. Pseudocapacitive Electrodes Produced by Oxidant-Free Polymerization of Pyrrole between the Layers of 2D Titanium Carbide (MXene). *Adv. Mater.* **2016**, *28*, 1517–1522. [CrossRef]
11. Xu, J.; Hu, X.; Wang, X.; Wang, X.; Ju, Y.; Ge, S.; Lu, X.; Ding, J.; Yuan, N.; Gogotsi, Y. Low-Temperature Pseudocapacitive Energy Storage in Ti_3C_2Tx MXene. *Energy Storage Mater.* **2020**, *33*, 382–389. [CrossRef]
12. Zhao, M.Q.; Ren, C.E.; Ling, Z.; Lukatskaya, M.R.; Zhang, C.; Van Aken, K.L.; Barsoum, M.W.; Gogotsi, Y. Flexible MXene/Carbon Nanotube Composite Paper with High Volumetric Capacitance. *Adv. Mater.* **2015**, *27*, 339–345. [CrossRef]
13. Yan, J.; Ren, C.E.; Maleski, K.; Hatter, C.B.; Anasori, B.; Urbankowski, P.; Sarycheva, A.; Gogotsi, Y. Flexible MXene/Graphene Films for Ultrafast Supercapacitors with Outstanding Volumetric Capacitance. *Adv. Funct. Mater.* **2017**, *27*, 1701264. [CrossRef]
14. Yan, J.; Ma, Y.; Zhang, C.; Li, X.; Liu, W.; Yao, X.; Yao, S.; Luo, S. Polypyrrole-MXene Coated Textile-Based Flexible Energy Storage Device. *RSC Adv.* **2018**, *8*, 39742–39748. [CrossRef] [PubMed]
15. Wu, W.; Wei, D.; Zhu, J.; Niu, D.; Wang, F.; Wang, L.; Yang, L.; Yang, P.; Wang, C. Enhanced Electrochemical Performances of Organ-like Ti 3 C 2 MXenes/Polypyrrole Composites as Supercapacitors Electrode Materials. *Ceram. Int.* **2019**, *45*, 7328–7337. [CrossRef]
16. Le, T.A.; Tran, N.Q.; Hong, Y.; Lee, H. Intertwined Titanium Carbide MXene within a 3 D Tangled Polypyrrole Nanowires Matrix for Enhanced Supercapacitor Performances. *Chem.—A Eur. J.* **2019**, *25*, 1037–1043. [CrossRef]
17. Liang, W.; Zhitomirsky, I. MXene-Polypyrrole Electrodes for Asymmetric Supercapacitors. *Electrochim. Acta* **2022**, *406*, 139843. [CrossRef]
18. Zhu, J.; Tang, Y.; Yang, C.; Wang, F.; Cao, M. Composites of TiO 2 Nanoparticles Deposited on Ti 3 C 2 MXene Nanosheets with Enhanced Electrochemical Performance. *J. Electrochem. Soc.* **2016**, *163*, A785–A791. [CrossRef]
19. Nagarajan, R.D.; Sundaramurthy, A.; Sundramoorthy, A.K. Synthesis and Characterization of MXene (Ti_3C_2Tx)/Iron Oxide Composite for Ultrasensitive Electrochemical Detection of Hydrogen Peroxide. *Chemosphere* **2022**, *286*, 131478. [CrossRef]
20. Wei, Y.; Zheng, M.; Luo, W.; Dai, B.; Ren, J.; Ma, M.; Li, T.; Ma, Y. All Pseudocapacitive MXene-MnO_2 Flexible Asymmetric Supercapacitor. *J. Energy Storage* **2022**, *45*, 103715. [CrossRef]
21. Shen, B.; Huang, H.; Jiang, Y.; Xue, Y.; He, H. 3D Interweaving MXene–Graphene Network–Confined Ni–Fe Layered Double Hydroxide Nanosheets for Enhanced Hydrogen Evolution. *Electrochim. Acta* **2022**, *407*, 139913. [CrossRef]
22. Zhang, R.; Dong, J.; Zhang, W.; Ma, L.; Jiang, Z.; Wang, J.; Huang, Y. Synergistically Coupling of 3D FeNi-LDH Arrays with Ti3C2Tx-MXene Nanosheets toward Superior Symmetric Supercapacitor. *Nano Energy* **2022**, *91*, 106633. [CrossRef]
23. Liang, W.; Zhitomirsky, I. MXene-Carbon Nanotube Composite Electrodes for High Active Mass Asymmetric Supercapacitors. *J. Mater. Chem. A Mater.* **2021**, *9*, 10335–10344. [CrossRef]
24. Yi, H.; Pang, S.; Yang, G.; Yao, X.; Li, C.; Jiang, J.; Li, Y. MXene Modified Carbon Fiber Composites with Improved Mechanical Properties Based on Electrophoretic Deposition. *Mater. Res. Bull.* **2022**, *150*, 111761. [CrossRef]
25. Wen, D.; Ying, G.; Liu, L.; Li, Y.; Sun, C.; Hu, C.; Zhao, Y.; Ji, Z.; Zhang, J.; Wang, X. Direct Inkjet Printing of Flexible MXene/Graphene Composite Films for Supercapacitor Electrodes. *J. Alloy. Compd.* **2022**, *900*, 163436. [CrossRef]
26. Zeng, Y.; Yu, M.; Meng, Y.; Fang, P.; Lu, X.; Tong, Y. Iron-Based Supercapacitor Electrodes: Advances and Challenges. *Adv. Energy Mater.* **2016**, *6*, 1601053. [CrossRef]
27. Li, Y.; Hu, N. Modification of the Elemental Composition of Iron(III) Oxide as an Asymmetric Supercapacitor Anode: A Minireview. *Instrum. Sci. Technol.* **2020**, *48*, 637–666. [CrossRef]

28. Li, J.; Chen, D.; Wu, Q. α-Fe_2O_3 Based Carbon Composite as Pure Negative Electrode for Application as Supercapacitor. *Eur. J. Inorg. Chem.* **2019**, *2019*, 1301–1312. [CrossRef]
29. Tufa, L.T.; Gicha, B.B.; Wu, H.; Lee, J. Fe-Based Mesoporous Nanostructures for Electrochemical Conversion and Storage of Energy. *Batter. Supercaps* **2021**, *4*, 429–444. [CrossRef]
30. Ma, J.; Guo, X.; Yan, Y.; Xue, H.; Pang, H. FeO_x-Based Materials for Electrochemical Energy Storage. *Adv. Sci.* **2018**, *5*, 1700986. [CrossRef]
31. Ma, Y.; Sheng, H.; Dou, W.; Su, Q.; Zhou, J.; Xie, E.; Lan, W. Fe_2O_3Nanoparticles Anchored on the $Ti_3C_2T_x$MXene Paper for Flexible Supercapacitors with Ultrahigh Volumetric Capacitance. *ACS Appl. Mater. Interfaces* **2020**, *12*, 41410–41418. [CrossRef] [PubMed]
32. Zhao, K.; Wang, H.; Zhu, C.; Lin, S.; Xu, Z.; Zhang, X. Free-Standing MXene Film Modified by Amorphous FeOOH Quantum Dots for High-Performance Asymmetric Supercapacitor. *Electrochim. Acta* **2019**, *308*, 1–8. [CrossRef]
33. Li, F.; Liu, Y.L.; Wang, G.G.; Zhang, H.Y.; Zhang, B.; Li, G.Z.; Wu, Z.P.; Dang, L.Y.; Han, J.C. Few-Layered Ti_3C_2T: X MXenes Coupled with Fe_2O_3 Nanorod Arrays Grown on Carbon Cloth as Anodes for Flexible Asymmetric Supercapacitors. *J. Mater. Chem. A Mater.* **2019**, *7*, 22631–22641. [CrossRef]
34. Fan, Z.; Wang, Y.; Xie, Z.; Xu, X.; Yuan, Y.; Cheng, Z.; Liu, Y. A Nanoporous MXene Film Enables Flexible Supercapacitors with High Energy Storage. *Nanoscale* **2018**, *10*, 9642–9652. [CrossRef] [PubMed]
35. Li, H.; Liu, Y.; Lin, S.; Li, H.; Wu, Z.; Zhu, L.; Li, C.; Wang, X.; Zhu, X.; Sun, Y. Laser Crystallized Sandwich-like MXene/Fe_3O_4/MXene Thin Film Electrodes for Flexible Supercapacitors. *J. Power Sources* **2021**, *497*, 229882. [CrossRef]
36. Wang, Y.; Li, Y.; Qiu, Z.; Wu, X.; Zhou, P.; Zhou, T.; Zhao, J.; Miao, Z.; Zhou, J.; Zhuo, S. Fe_3O_4@Ti_3C_2 MXene Hybrids with Ultrahigh Volumetric Capacity as an Anode Material for Lithium-Ion Batteries. *J. Mater. Chem. A Mater.* **2018**, *6*, 11189–11197. [CrossRef]
37. Zhang, C.; Xu, S.; Cai, D.; Cao, J.; Wang, L.; Han, W. Planar Supercapacitor with High Areal Capacitance Based on Ti_3C_2/Polypyrrole Composite Film. *Electrochim. Acta* **2020**, *330*, 135277. [CrossRef]
38. Wu, W.; Niu, D.; Zhu, J.; Gao, Y.; Wei, D.; Zhao, C.; Wang, C.; Wang, F.; Wang, L.; Yang, L. Hierarchical Architecture of Ti_3C_2@PDA/$NiCo_2S_4$ Composite Electrode as High-Performance Supercapacitors. *Ceram. Int.* **2019**, *45*, 16261–16269. [CrossRef]
39. Oyedotun, K.O.; Momodu, D.Y.; Naguib, M.; Mirghni, A.A.; Masikhwa, T.M.; Khaleed, A.A.; Kebede, M.; Manyala, N. Electrochemical Performance of Two-Dimensional Ti_3C_2-Mn_3O_4 Nanocomposites and Carbonized Iron Cations for Hybrid Supercapacitor Electrodes. *Electrochim. Acta* **2019**, *301*, 487–499. [CrossRef]
40. Wang, X.; Li, H.; Li, H.; Lin, S.; Ding, W.; Zhu, X.; Sheng, Z.; Wang, H.; Zhu, X.; Sun, Y. 2D/2D 1T-MoS_2/Ti_3C_2 MXene Heterostructure with Excellent Supercapacitor Performance. *Adv. Funct. Mater.* **2020**, *30*, 1–11. [CrossRef]
41. Zheng, S.; Zhang, C.; Zhou, F.; Dong, Y.; Shi, X.; Nicolosi, V.; Wu, Z.S.; Bao, X. Ionic Liquid Pre-Intercalated MXene Films for Ionogel-Based Flexible Micro-Supercapacitors with High Volumetric Energy Density. *J. Mater. Chem. A Mater.* **2019**, *7*, 9478–9485. [CrossRef]
42. Tian, Y.; Que, W.; Luo, Y.; Yang, C.; Yin, X.; Kong, L.B. Surface Nitrogen-Modified 2D Titanium Carbide (MXene) with High Energy Density for Aqueous Supercapacitor Applications. *J. Mater. Chem. A Mater.* **2019**, *7*, 5416–5425. [CrossRef]
43. Chen, R.; Yu, M.; Sahu, R.P.; Puri, I.K.; Zhitomirsky, I. The Development of Pseudocapacitor Electrodes and Devices with High Active Mass Loading. *Adv. Energy Mater.* **2020**, *10*, 1903848. [CrossRef]
44. Gogotsi, Y.; Simon, P. True Performance Metrics in Electrochemical Energy Storage. *Science* **2011**, *334*, 917–918. [CrossRef] [PubMed]
45. Wang, H.; Holt, C.M.B.; Li, Z.; Tan, X.; Amirkhiz, B.S.; Xu, Z.; Olsen, B.C.; Stephenson, T.; Mitlin, D. Graphene-Nickel Cobaltite Nanocomposite Asymmetrical Supercapacitor with Commercial Level Mass Loading. *Nano Res.* **2012**, *5*, 605–617. [CrossRef]
46. Liao, J.; Li, Y.; Wang, Z.; Lv, L.; Chang, L. In-Situ Preparation of Fe_3O_4/Graphene Nanocomposites and Their Electrochemical Performances for Supercapacitor. *Mater. Chem. Phys.* **2021**, *258*, 123995. [CrossRef]
47. Nguyen, M.D.; Tran, H.V.; Xu, S.; Lee, T.R. Fe_3O_4 Nanoparticles: Structures, Synthesis, Magnetic Properties, Surface Functionalization, and Emerging Applications. *Appl. Sci.* **2021**, *11*, 11301. [CrossRef]
48. Serga, V.; Burve, R.; Maiorov, M.; Krumina, A.; Skaudžius, R.; Zarkov, A.; Kareiva, A.; Popov, A.I. Impact of Gadolinium on the Structure and Magnetic Properties of Nanocrystalline Powders of Iron Oxides Produced by the Extraction-Pyrolytic Method. *Materials* **2020**, *13*, 4147. [CrossRef]
49. Liang, W.; Zhitomirsky, I. Composite Fe_3O_4-Mxene-Carbon Nanotube Electrodes for Supercapacitors Prepared Using the New Colloidal Method. *Materials* **2021**, *14*, 2930. [CrossRef]
50. Zhu, Y.; Shi, K.; Zhitomirsky, I. Polypyrrole Coated Carbon Nanotubes for Supercapacitor Devices with Enhanced Electrochemical Performance. *J. Power Sources* **2014**, *268*, 233–239. [CrossRef]
51. Zhang, Y.; Cui, X.; Fu, J.; Liu, Y.; Wu, Y.; Zhou, J.; Zhang, Z.; Xie, E. Commercial-Level Mass-Loading $MnO_2$with Ion Diffusion Channels for High-Performance Aqueous Energy Storage Devices. *J. Mater. Chem. A Mater.* **2021**, *9*, 17945–17954. [CrossRef]
52. Wang, Y.; Liu, Y.; Zhitomirsky, I. Surface Modification of MnO_2 and Carbon Nanotubes Using Organic Dyes for Nanotechnology of Electrochemical Supercapacitors. *J. Mater. Chem. A Mater.* **2013**, *1*, 12519–12526. [CrossRef]
53. Zang, X.; Wang, J.; Qin, Y.; Wang, T.; He, C.; Shao, Q.; Zhu, H.; Cao, N. Enhancing Capacitance Performance of $Ti_3C_2T_x$ MXene as Electrode Materials of Supercapacitor: From Controlled Preparation to Composite Structure Construction. *Nanomicro Lett.* **2020**, *12*, 77. [CrossRef] [PubMed]

54. Li, R.; Liu, J. Mechanistic Investigation of the Charge Storage Process of Pseudocapacitive Fe_3O_4 Nanorod Film. *Electrochim. Acta* **2014**, *120*, 52–56. [CrossRef]
55. Yewale, M.A.; Kadam, R.A.; Kaushik, N.K.; Nguyen, L.N.; Nakate, U.T.; Lingamdinne, L.P.; Koduru, J.R.; Auti, P.S.; Vattikuti, S.V.P.; Shin, D.K. Electrochemical Supercapacitor Performance of $NiCo_2O_4$ Nanoballs Structured Electrodes Prepared via Hydrothermal Route with Varying Reaction Time. *Colloids Surf. A Physicochem. Eng. Asp.* **2022**, *653*, 129901. [CrossRef]
56. Yewale, M.A.; Kadam, R.A.; Kaushik, N.K.; Linh, N.N.; Teli, A.M.; Shin, J.C.; Lingamdinne, L.P.; Koduru, J.R.; Shin, D.K. Mesoporous Hexagonal Nanorods of $NiCo_2O_4$ Nanoparticles via Hydrothermal Route for Supercapacitor Application. *Chem. Phys. Lett.* **2022**, *800*, 139654. [CrossRef]
57. Yewale, M.A.; Kadam, R.A.; Kaushik, N.K.; Koduru, J.R.; Velhal, N.B.; Nakate, U.T.; Jadhavar, A.A.; Sali, N.D.; Shin, D.K. Interconnected Plate-like $NiCo_2O_4$ Microstructures for Supercapacitor Application. *Mater. Sci. Eng. B. Solid. State Mater. Adv. Technol.* **2023**, *287*, 116072. [CrossRef]
58. Mariappan, V.K.; Krishnamoorthy, K.; Pazhamalai, P.; Natarajan, S.; Sahoo, S.; Nardekar, S.S.; Kim, S.J. Antimonene Dendritic Nanostructures: Dual-Functional Material for High-Performance Energy Storage and Harvesting Devices. *Nano Energy* **2020**, *77*, 105248. [CrossRef]
59. Okhay, O.; Tkach, A. Graphene/Reduced Graphene Oxide-Carbon Nanotubes Composite Electrodes: From Capacitive to Battery-Type Behaviour. *Nanomaterials* **2021**, *11*, 1240. [CrossRef]
60. Liang, W. Advanced Electrode Materials and Fabrication of Supercapacitors. 2022. Available online: http://hdl.net/11375/27386 (accessed on 1 December 2022).
61. Zhang, L.; Wang, Z.; Chen, W.; Yuan, R.; Zhan, K.; Zhu, M.; Yang, J.; Zhao, B. Fe3O4nanoplates Anchored on Ti3C2T: XMXene with Enhanced Pseudocapacitive and Electrocatalytic Properties. *Nanoscale* **2021**, *13*, 15343–15351. [CrossRef]
62. Zhang, L.; Yu, K.; Li, Y.; Wang, Z.; Zhan, K.; Yang, J.; Zhao, B. Nanoparticles of Fe_3O_4 Anchored on Ti3C2Tx MXene/RGO Aero gels as Hybrid Negative Electrodes for Advanced Supercapacitors. *ACS Appl. Nano Mater.* **2023**, *6*, 482–491. [CrossRef]